DOI: 10.1002/ejic.200701173

Structural, Magnetic and Magnetotransport Properties of $La_{0.7}Pb_{0.3}(Mn_{1-x}Ni_x)O_3$ ($0.1 \leq x \leq 0.3$) CMR Manganites

Alazne Peña,[a] Jon Gutiérrez,*[b] Javier Campo,[c][‡] Jose Manuel Barandiarán,[b] Luis Lezama,[a] Izaskun Gil de Muro,[a] and Teófilo Rojo[a]

Keywords: Manganites / Crystal structure / Neutron diffraction / Magnetization / Magnetoresistance / Metal–insulator transition

Structural and magnetic properties of $La_{0.7}Pb_{0.3}(Mn_{1-x}Ni_x)O_3$ ($0.1 \leq x \leq 0.3$) manganites are reported. Samples were fabricated by the sol–gel low-temperature method. At room temperature, the first structural characterization of all phases indicated the rhombohedral space group ($R\bar{3}c$). All compositions show ferromagnetic behaviour and magnetoresistance. The measured low-temperature magnetic moment and the Curie temperature continuously decrease, with respect to the undoped composition, as Mn ions are substituted progressively by Ni. This is interpreted in terms of direct substitution of Mn^{3+} by low-spin (LS) Ni^{3+} ions. The measured magnetoresistance reaches 46 % for the 10 % Ni-doped composition and 28 % for the 30 % Ni-doped one at the corresponding Curie temperature. The resistivity behaviour of all the studied compounds is fully determined by the intergrain conduction mechanism, with grain sizes in the range 20–45 nm.

Introduction

The continuous interest exhibited by the scientific community in the perovskite-like phases with the general formula $Ln^{3+}_{1-x}M^{2+}_xMnO_3$ (Ln^{3+} = La, Pr, Nd, Sm... and M^{2+} = Ca, Sr, Ba, Pb...) is mainly due to the magnetotransport properties exhibited[1,2] by this type of compounds. Our current view of the electronic structure of these materials, upon which the double exchange (DE) mechanism[3] rests, portrays a strong on-site exchange interaction (Hund's rule couple $J \approx 2$–3 eV[4]) between the localized t_{2g} spins and itinerant e_g electrons.[5] This mechanism is used to explain the ferromagnetic behaviour of these phases, while the simultaneous presence of ferromagnetism and the metallic state brings about colossal magnetoresistance (CMR) when the magnetic field is changed.[6] The rhombohedral and orthorhombic distortion of the actual crystallographic structure of classic cubic symmetry is also an essential factor in understanding the magnetic and transport properties of these samples.[7] The composition $La_{0.7}A_{0.3}MnO_3$ corresponds to a Mn^{3+}/Mn^{4+} ratio that maximizes the DE interaction and shows ferromagnetism and CMR. Choosing A as Sr or Pb raises the magnetic order temperatures (T_C = 345 K for $La_{0.7}Pb_{0.3}MnO_3$) relative to the prototype composition containing Ca (for which T_C = 265 K).

Thus, the transport and magnetic properties of these materials are known to be strongly dependent upon changes in the strength of the DE interaction. This can also be altered by the substitution of the Mn ions by other transition-metal ions in the form $Ln_{0.7}A_{0.3}Mn_{1-y}TM^{3+}_yO_3$ (TM: transition metal), with important modifications in their magnetic and transport properties.[8–12] In this sense, the effect of substituting different trivalent ions from the iron group (partially filled 3d shells) such as Fe^{3+} ($3d^5$), Co^{3+} ($3d^6$) or Ni^{3+} ($3d^7$) in the Mn site is still an interesting subject.

We have shown, in previous studies,[8,13] that iron enters as high-spin $t_{2g}^3e_g^2$ (HS, S = 5/2) Fe^{3+} into the $La_{0.7}Pb_{0.3}Mn_{1-x}Fe_xO_3$ family of compositions, because this is the most stable oxidation state for this cation and its ionic radius is very similar to that of the Mn^{3+} ion. Iron couples antiferromagnetically with Mn ions and weakens progressively the double exchange mechanism and therefore the ferromagnetic character (decrease in both Curie temperature and low-temperature magnetic moment values) of the compounds as the doping level increases. A 20–30 % substitution of Fe leads to magnetic frustration and insulating behaviour in these compositions.

When the dopant cation used is cobalt (that is $Mn_{1-x}Co_x$) in percentages up to x = 0.3, our previous studies indicate that again the entrance of this element causes

[a] Universidad del País Vasco/EHU, Facultad de Ciencia y Tecnología, Dpto. de Química Inorgánica,
Apartado 644, 48080 Bilbao, Spain
Fax: +34-94-601-35-00
E-mail: alazne.pena@ehu.es
[b] Dpto. de Electricidad y Electrónica – Un. As. CSIC, Fac. de Ciencia y Tecnología, Univ. del País Vasco/EHU,
Apdo. 644, 48080 Bilbao, Spain
[c] Institut Laue Langevin (ILL, CRG-D1B),
Rue Jules Horowitz, B. P. 156, 38042 Grenoble Cedex 9, France
[‡] Present address: Instituto de Ciencia de los Materiales de Aragón, Universidad de Zaragoza – CSIC, Facultad de Ciencias
50009 Zaragoza, Spain

low distortion in the perovskite structure, with a mixture of low-spin Co^{3+} and high-spin Co^{4+}.[14] These compounds show a clear trend towards cluster glass behaviour probably because Co^{3+} clusters around Co^{4+} ions.

The most stable Ni ion configurations are the high-spin Ni^{2+}, $t_{2g}^6e_g^2$ (HS, $S = 1$) and the low-spin Ni^{3+}, $t_{2g}^6e_g^1$ (LS, $S = 1/2$). This last ion as well as Mn^{3+} ($t_{2g}^3e_g^1$) are Jahn–Teller ions with a single e_g electron with crystal degeneracy. Early work by Goodenough et al.[15] reported ternary oxides $LaMn_{1-x}Ni_xO_3$ to be ferromagnets in the range up to $x = 0.5$. Blasse suggested this ferromagnetism to be governed by the positive superexchange interaction between Ni^{2+} and Mn^{4+} ions through oxygen anions.[16] However, other studies performed on this series provided different conclusions about the electronic state of Ni and Mn: while some authors claimed that there was a homovalent substitution between Ni^{3+} and Mn^{3+},[17] others reported the presence of Ni^{2+} and Mn^{4+} ions.[16,18] A quite complete study performed by Blasco et al.[19] demonstrated that Ni and Mn are mainly in a mixed-valence state along the $LaNi_{1-x}Mn_xO_3$ ($x = 0.1$ to 0.9) series.

In this work we present the magnetic and structural properties of the $La_{0.7}Pb_{0.3}(Mn_{1-x}Ni_x)O_3$ manganites when Mn is substituted progressively by Ni up to 30% doping levels. Neutron diffraction, magnetic and transport measurements and the electron spin resonance technique have been used in order to perform this study. We were especially careful in the analysis of the structural properties of the studied compositions and tried to explain the observed magnetic and magnetotransport properties on the basis of the previously determined structural properties.

Results and Discussion

The crystal structure of this family of compounds has been analyzed in the trigonal space group ($R\bar{3}c$) (see Figure 1), hexagonal setting ($Z = 6$), by using D1B neutron powder diffraction data. All structural parameters obtained from neutron diffraction experiments together with the tolerance factor (t) of the perovskite structure, $t = (d\text{La–O})/\sqrt{2}(d\text{Mn–O})$ (where dLa–O and dMn–O are the corresponding bond lengths) are summarized in Table 3. Our previous study[13] on the related parent compound $La_{0.7}Pb_{0.3}MnO_3$ gave as the main structural parameters the following: $V = 353.01$ Å^3, $t = 0.995$, ∠Mn–O–Mn = 166.8° and ∠O–Mn–O = 90.71°. We have observed that for our compounds the unit-cell volume decreases with increasing Ni content. Nevertheless, the substitution of Mn by Ni produces only a minor distortion in the MnO_6 octahedra, and the O–Mn–O and Mn–O–Mn angles remain rather constant. The tolerance factor does not suffer any appreciable change for the different compositions. These geometrical characteristics indicate that the distortion of the $La_{0.7}Pb_{0.3}Mn_{1-x}Ni_xO_3$ perovskite structure is nearly independent of the x value, this being in good agreement with the comparable size of the Mn^{3+} ($<r_{Mn}> = 0.785$ Å) and Ni^{3+} (LS, with $<r_{Ni}> = 0.7155$ Å) ions.[20]

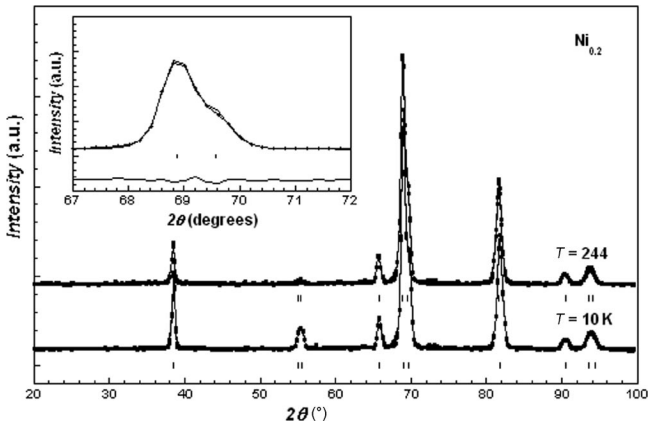

Figure 1. Rietveld fit to the neutron diffraction data (recorded above and below T_C) for the compound $La_{0.7}Pb_{0.3}Mn_{0.8}Ni_{0.2}O_3$ showing Bragg reflections for the ($R\bar{3}c$) phase and (inset) refinement of the main diffraction peak, around $2\theta = 69°$.

The thermal evolution of the neutron diffraction patterns for these samples was also recorded. In all cases, two reflections with magnetic contribution at the same d values are observed. This feature is indicative of an equivalent magnetic structure for the compounds. That is, the magnetic order does not change its structure when 10, 20 or 30% Ni is included in these La-based phases. Furthermore, all magnetic reflections can be indexed with the same cell as the nuclear one, indicating an equivalent type of ferromagnetic structure with collinear magnetic moments. The magnetic contribution appears at about 280, 240 and 225 K for the 10, 20 and 30% Ni-doped compositions, respectively. The best solution for the fits was obtained with a collinear magnetic structure in which the magnetic moment of the Mn ion is placed into the (110) crystallographic plane, in the hexagonal setting (perpendicular to the [111] direction of the perovskite cubic cell). The obtained values of the magnetic moment at the lowest temperature of the measurement (1.5 K or 10 K) are 2.62, 2.41 and 2.21 μ_B for the 10, 20 and 30% Ni-doped compositions, respectively. Figure 2

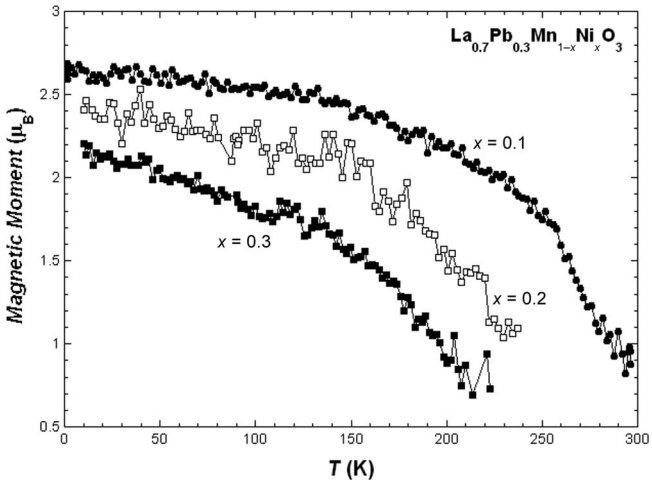

Figure 2. Temperature dependence of the magnetic moment obtained from neutron diffraction data for the Ni family of compounds.

shows the temperature dependence of the refined magnetic moment value for the Ni-containing compositions.

The oxygen stoichiometry of the samples was determined by thermogravimetric analysis, by heating the oxides up to 900 °C in flowing 5% H_2/Ar. The samples were reduced to MnO and Ni, and the observed weight losses allowed us to determine a slight oxygen deficiency. In this way, we determined the studied samples to be of compositions $La_{0.7}Pb_{0.3}Mn_{0.9}Ni_{0.1}O_{2.95}$, $La_{0.7}Pb_{0.3}Mn_{0.8}Ni_{0.2}O_{2.95}$ and $La_{0.7}Pb_{0.3}Mn_{0.7}Ni_{0.3}O_{2.89}$. This observed oxygen deficiency is in good agreement with the quantities obtained from the redox titration, in all cases.

Two consecutive weight losses for all the samples are observed as temperature increases (see Figure 3). The first loss occurs at approximately 450 °C, while the second loss happens at approximately 550 °C, the same temperatures in all cases. According to this we can affirm that first, the Mn^{4+} and Ni^{3+} ions are reduced to Mn^{3+} and Ni^{2+}, respectively, and when all components appear in the form Mn^{3+} and Ni^{2+}, the second reduction takes place, that is to say, the Mn^{3+} and Ni^{2+} ions are reduced to Mn^{2+} and Ni, respectively.[21]

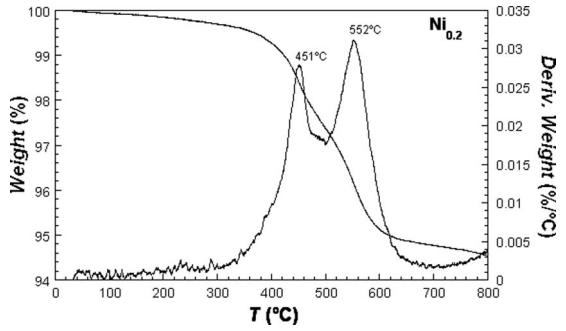

Figure 3. Thermogravimetric curve in H_2 for the sample containing 20% Ni (curves for all compositions are similar). It shows two steps indicating the reduction processes $TM^{4+} \rightarrow TM^{3+} \rightarrow TM^{2+}$ (TM = Mn and Ni).

In Figure 4 the zero-field cooling (ZFC) and field cooling (FC) curves obtained for all the compositions are shown. We[13] determined the following values for the undoped $La_{0.7}Pb_{0.3}MnO_3$ composition: low-temperature magnetic moment $<\mu_{Mn}>_{LT} = 3.4\ \mu_B$, Curie temperature $T_C = 345$ K and high-temperature effective moment $<\mu_{Mn}>_{HT} = 5.9\ \mu_B$. From ZFC curves, a continuous decrease in the magnetic order or Curie temperature from 265 K for the 10% Ni-doped composition to 205 K for the 30% Ni-doped one is clearly observed. There is a remarkable similarity between this low-field magnetization behaviour, indicating that the magnetization process is basically the same. The degree of irreversibility of such processes is low, as indicated by the splitting between ZFC and FC curves. This bifurcation of both curves occurs at a temperature T_b corresponding to the blocking temperature of the largest particles in the assembly. That is, T_b defines also a temperature above which magnetization processes are fully reversible.

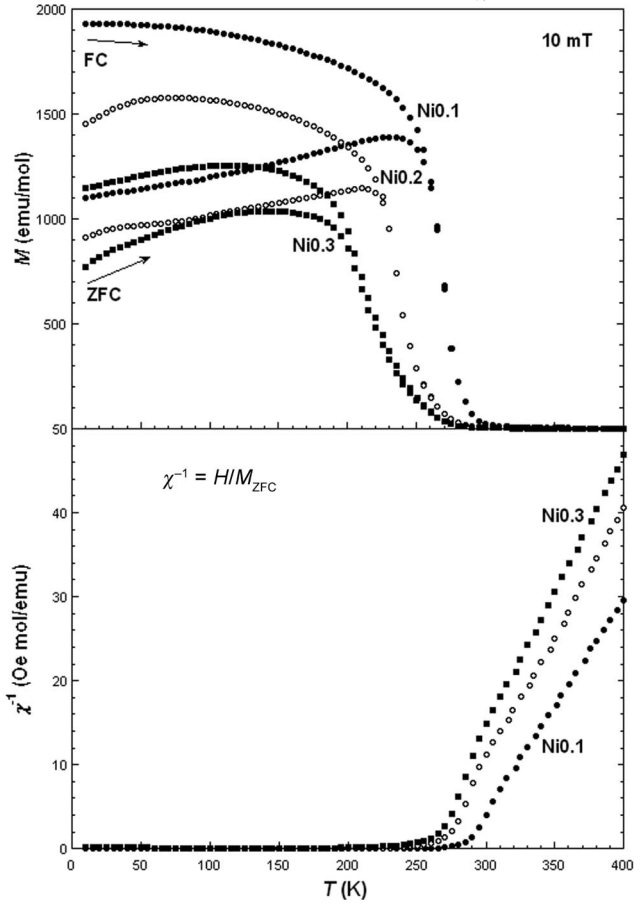

Figure 4. Zero-field cooling (ZFC) and field cooling (FC) curves measured at 10 mT (upper frame) and deduced χ^{-1}_{dc} behaviour from ZFC curves (lower frame).

The hysteresis loops, measured at 10 K and up to 7 Tesla (see Figure 5), show the usual ferromagnetic behaviour, quickly reaching magnetic saturation already for applied fields of 3 Tesla. The measured coercitivity continuously increases as the Ni content in the sample increases, with values of 5.6, 8.7 and 9.5 kA/m for the 10, 20 and 30% Ni-containing samples, respectively. The experimental value of the low-temperature magnetic moment was also determined by using Arrott plots.[22] Thus, all samples exhibit a continuous decrease in the saturation magnetization as the percentage of doping ion increases. All the measured magnetic and magnetotransport data are summarized in Tables 1 and 2. The obtained values of the low-temperature magnetic moment closely correlate with the expected theoretical values $<\mu>_{LT} = (1 - x)<\mu_{Mn}>_{LT} + x<\mu_{Ni}>_{LT}$, when we have assumed, as previously, that Ni enters as Ni^{3+} (LS) contributing with only 1 μ_B to the magnetic moment. If we compare values for the low-temperature magnetic moment appearing in Table 1, we will notice that the magnetic moment determined by using neutron diffraction measurements is in all cases lower than that determined by means of macroscopic magnetic measurements, where the properties of the bulk are measured. This kind of discrepancy has already been observed in other compounds containing 3d elements

Table 1. Values of the Curie temperature, low-temperature magnetic moment (from magnetic and neutron diffraction measurements), expected low-temperature magnetic moment value, blocking temperature, effective and expected high-temperature magnetic moment values and paramagnetic Curie temperature, for the $La_{0.7}Pb_{0.3}(Mn_{1-x}Ni_x)O_3$ ($0.1 \leq x \leq 0.3$) family of compounds.

Sample	T_C (K)[a]	μ (μ_B)[a]	μ_{ex} (μ_B)	T_{ord} (K)[b]	μ (μ_B)[b]	T_b (K)	μ_{eff} (μ_B)[e]	θ_C (K)[e]	μ_t (μ_B)[f]
Ni0.1	265	3.11	3.16	280	2.62[c]	260	5.59	283	5.61
Ni0.2	230	2.98	2.92	240	2.41[d]	230	5.21	264	5.29
Ni0.3	205	2.77	2.68	225	2.21[d]	240	4.98	255	4.96

[a] Values obtained from bulk magnetic measurements. [b] Values obtained from neutron diffraction measurements. [c] T = 1.5 K. [d] T = 10 K. [e] Values from the Curie–Weiss law in the paramagnetic regime. [f] Values calculated as explained in the text.

where the magnetic atom is octahedrally coordinated[23] and has been explained on the basis of magnetic moment delocalization between the 3d element and the ligands. As a result of this delocalization, the magnetic moment value measured by unpolarized neutron diffraction, which is only sensitive to the magnetic moment in the 3d-element site (and not in its vicinity), is lower than the real one. Moreover, macroscopic measurements by using SQUID magnetometry give the total magnetic moment, localized and not localized.

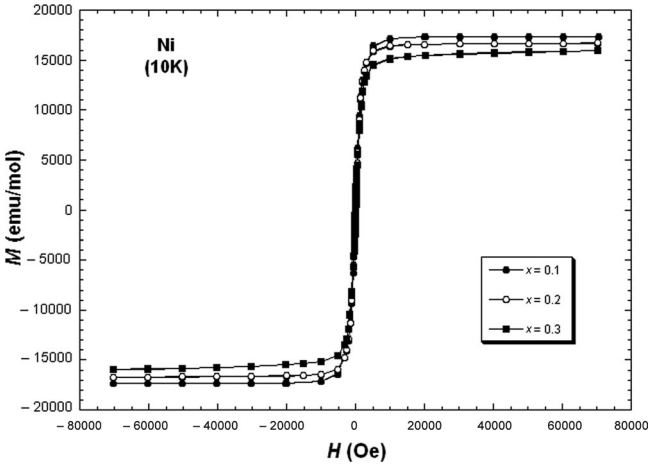

Figure 5. Hysteresis loops measured at 10 K and up to 7 Tesla.

Table 2. Values of magnetoresistance for H = 6 T at the corresponding Curie temperature, calculated energy gap from Mott's law, temperature of the minimum of the resonance linewidth, resistivity at room temperature and activation energy values for the $La_{0.7}Pb_{0.3}(Mn_{1-x}Ni_x)O_3$ ($0.1 \leq x \leq 0.3$) family of compounds.

Sample	MR (%)	ΔE (eV)[a]	θ_{min} (K)	ρ (Ω cm)	ΔE (eV)[b]
Ni0.1	46	0.9	305	0.07	0.24
Ni0.2	32	4.4	265	0.63	0.18
Ni0.3	28	4.8	255	12.7	0.16

[a] Data fitted to the variable range hopping model [Equation (1)], $T > T_C$ range. [b] Data fitted to the Arrhenius law [Equation (4)], in the paramagnetic regime.

We can check the validity of our guess that Ni enters the samples as Ni^{3+} (LS with 1 μ_B) by analyzing the $\chi^{-1}_{dc} = H/M_{ZFC}$ vs. T behaviour measured in the paramagnetic phase for the different samples. A Curie–Weiss law is clearly followed above T_C and in the temperature range over which the data were taken (see Figure 4). The effective moments, μ_{eff}, obtained from the Curie constants are shown in Table 1 together with the obtained paramagnetic Curie temperatures, θ_C. We have also calculated the expected value, μ_t, of that effective moment as $\mu_t = [(1 - x)<\mu \times \mu_{Mn}>^2_{HT} + x<\mu_{Ni}>^2_{HT}]^{1/2}$. The good agreement between measured and calculated effective magnetic moment values in the paramagnetic regime confirms our supposition about the electronic state of the Ni ion.

The values of the resistivity measured at room temperature are 0.07, 0.63 and 12.7 Ω cm for the 10, 20 and 30% Ni-containing samples, respectively. As expected, the conductivity of the samples decreases as the amount of Ni that enters in the composition of the samples increases.

From the measured resistivity values as a function of temperature and applied magnetic field, we can calculate the magnetoresistance as MR (%) = [1 – R(6 T)/R(0 T)]×100. The magnitude of this magnetoresistance (see Figure 6) is about 28% for the 30% Ni-containing sample and reaches 46% for the 10% Ni containing one, at the corresponding Curie temperature of each compound. As the doping level of Ni increases, a progressive decrease in the magnetoresistance (%) value (at the magnetic order temperature of each compound) has been observed (see Table 1).

It is already well established that the zero-field resistivity data obtained for $T > T_C$ obey the Mott variable range hopping (VRH) mechanism[24] when the carriers are localized near the Fermi energy, as it is in the case of hole-doped manganites. Previous studies[25,26] have determined that the exponent n = 1/2 is the most adequate one for this law. Indeed our zero-field resistance data obey Equation (1).

$$R(T) = R_0 \cdot exp\left(\frac{T_0}{T}\right)^{1/2} \quad (1)$$

Efros and Shklovskii[27] explained that such resistance behaviour is directly related to a form of hopping favoured by the Coulomb repulsion between carriers. Its most important consequence is the existence of an energy or Coulomb gap that basically reflects the differences between the minimum energies of adding an electron and subtracting one from the system, without disturbing the other charges. From the obtained T_0 values, we have estimated the values for these energy gaps to be in the range 1–5 eV (see Table 2). In particular, the sample containing a 20% doping element

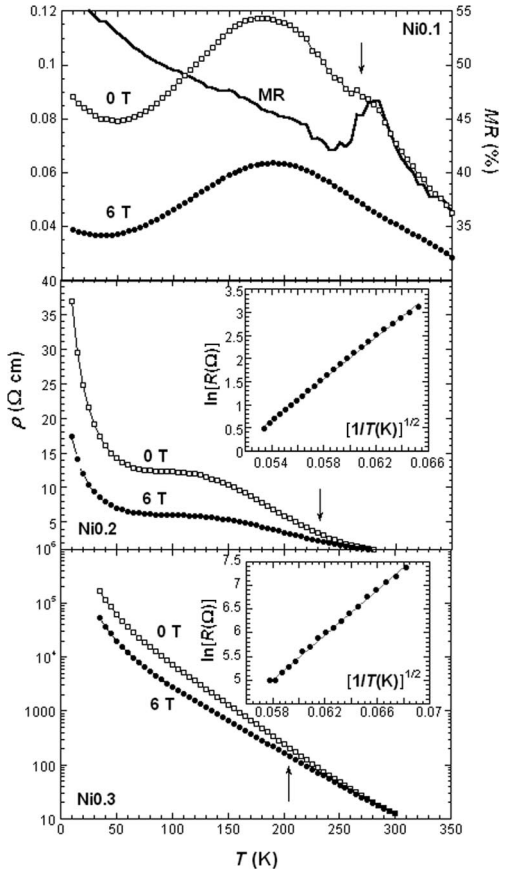

Figure 6. Temperature dependence of the electrical resistivity for all compounds (measured at 0 and 6 T applied magnetic field) as the doping level of Ni increases. The arrows indicate the corresponding Curie temperatures, of each sample. The insets show the magnetoresistance value (for $x = 0.1$) and the fit to the VRH law (for $x = 0.2$ and 0.3).

exhibits a gap value that is higher than the one obtained for $Ln_{0.7}A_{0.3}MnO_3$ type perovskites synthesized by using the ceramic method.[28,29] Other authors have already identified such resistivity behaviour, especially at low temperatures, as arising in samples of compounds with low grain size, (around 20–30 nm).[30] This can be also our case, since perovskites prepared by the sol–gel method present as one of their characteristics the fine grain obtained, typically below 1 μm.[31] It is already well established that tunnelling of electric charge into small nanoparticles increases the Coulomb energy by the charging effect, which strongly enhances the tunnel resistance. The grain sizes of our compounds can also be estimated by using the measured values of the blocking temperature. This can be written as $T_b = KV/(25k_B)$, where K is the anisotropy constant, V is the grain volume [$V = (3\pi/4)(d/2)^3$, d being the diameter of the grains, assumed to be spherical for simplicity]. From ferromagnetic resonance experiments in a similar $La_{0.67}Ba_{0.33}MnO_3$ oxide,[32] we used K values in the range $2–4 \times 10^{-2}$ J/cm^3. Thus, from the value of $T_b = 260$ K (10% Ni, the highest one), we inferred grain sizes of 20–25 nm for the compositions, in good agreement with the grain sizes obtained from our structural study. However, the presence of those nanosized grains in our samples is strongly supported also by the low-temperature behaviour of the resistivity of these compounds.

The 10% Ni-doped sample shows in its resistivity behaviour typical features of grain boundary effects, that is, a maximum of $\rho(T)$ at a temperature well below T_C which is not shifted to higher temperatures by applying an external magnetic field, and in particular a minimum of $\rho(T)$ at quite low temperatures, which gradually vanishes under external applied H (see Figure 7). The latter effect is due to spin-dependent tunnelling of carriers between grains. A simplified model to describe this situation gives Equation (2) for the resistivity.

$$\rho(T,H) = \frac{\rho_u}{1+\varepsilon\langle\cos\theta_{ij}\rangle} \tag{2}$$

where $\rho_u = r_0 + r_1 \cdot T^{3/2}$ (r_0 and r_1 being parameters independent of H), θ_{ij} is the angle between the magnetization directions of the grains, i and j, $<\cos\theta_{ij}> = -L(J/k_BT)$ when $H = 0$, $L(x) = \coth(x)–1/x$ is the Langevin function, and $\varepsilon = P^2$ indicates the degree of spin polarization of the carriers in each grain. A detailed description of this model can be found in ref.[33]

Figure 7 shows the low-temperature resistivity data for 10% Ni-doped compound. Data obtained under applied fields of 0 and 6 Tesla and the best fit obtained for the former are shown. This gives $\varepsilon = 0.479$, $r_0 = 0.0475\ \Omega$cm, $r_1 = 0.325 \times 10^{-4}\ \Omega$cm/K$^{3/2}$ and $J/k_B = 185$ K, which are of the same order as those given in ref.[33]

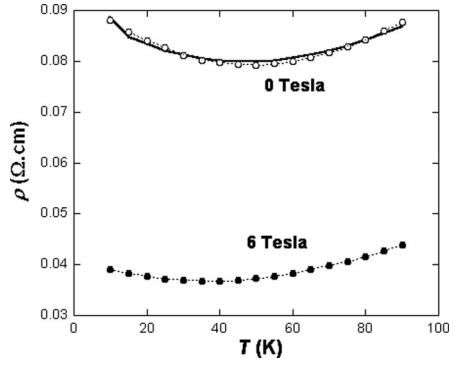

Figure 7. Low-temperature resistivity vs. temperature curves for the 10% Ni-doped sample. The solid line represents the obtained fit (see the text) of the data measured in the absence of an external applied magnetic field.

The 20% Ni-doped sample shows also the same characteristics, but at low temperatures and because of the small size of the grains, it is increasingly difficult to activate this intergrain mechanism. In this situation, transport is effectively blocked, giving as result a much higher upturn in the low-temperature resistivity. This is the so-called Coulomb blockade.[34]

Along this line of reasoning, our experimental data below 100 K fit well into the expression for granular metals [Equation (3)].[35]

$$\rho(T) \approx \exp\sqrt{(\Delta/T)} \quad (3)$$

where Δ is proportional to the activation or charging energy, E_C, of a single grain. From our fits we have obtained the value Δ = 5.6 K and a gap energy 2.7 meV for the 20% Ni-doped composition; these two values agree with results from other authors[30,36] obtained for related compounds. We also have to mention that the fit to the $T^{-1/2}$ law is better than the T^{-1} dependence postulated for the pure Coulomb blockade effect.

ESR and FMR spectra of the samples have been recorded above and below T_C. In all cases, only an averaged curve of the Mn/Ni spectra is detected. The measured room temperature spectra for all samples turn out to be quite narrow, a fact that indicates that the Ni ion present in the compositions is, actually, a Ni^{3+} ion. As expected, the Lorentzian-like narrow resonance signals obtained above the Curie temperature transform to asymmetric Dyson-like ones as the temperature decreases. When increasing the Ni content in these compounds, the FMR spectra for $T < T_C$ show single resonance but with large linewidths (see Figure 8). This is indicative of homogeneous distributions of magnetic grains (or spin clusters) of all sizes.

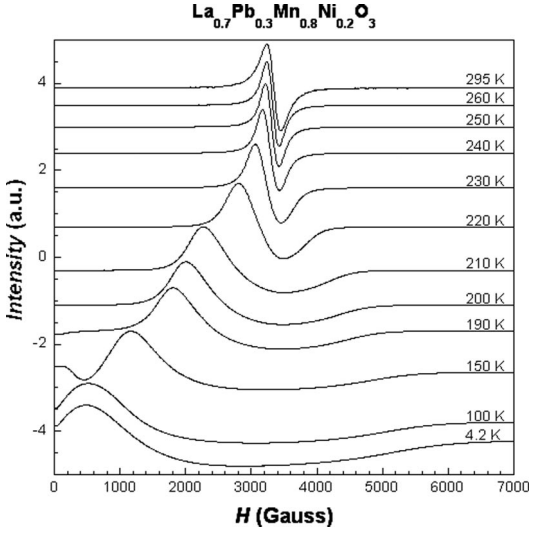

Figure 8. ESR spectra of the compound $La_{0.7}Pb_{0.3}Mn_{0.8}Ni_{0.2}O_3$ recorded at different temperatures.

As a function of T, the ESR linewidth (ΔH_{pp}) showed in all cases a behaviour similar to that described in previous studies:[37] ΔH_{pp} (T) decreases with decreasing temperature down to T_C. Analysis of the temperature dependence of the linewidth shows minima, θ_{min}, (at 305 K, 265 K and 255 K for x = 0.1, 0.2 and 0.3, respectively) that correlate directly with the obtained paramagnetic Curie temperatures (from the Curie–Weiss law), θ_C, for these compounds. Those temperatures are in all cases above the magnetic order ones (see Table 2). The value of θ_{min}, the measured linewidth at this temperature and especially the rate of increase below it have been reported to be extremely sample-dependent.[38] It has been subsequently suggested that this behaviour may be associated with some magnetic nonhomogeneity of the samples arising from local variations of chemical composition (arising in our case from the substitution of Mn by Ni ions) or the oxygen stoichiometry.[39]

For these Ni-doped compounds, the low value of the relaxation time spin lattice when increasing the temperature compensates the effect of the diminution of the interactions and gives rise to linewidths, at room temperature, that are practically equal for all compounds; there is only a slight increase from 183 to 218 G as the Ni content in the sample increases from 10 to 30%, respectively.

The value of the magnetic field for which the absorption is maximum displays a slight variation with the temperature above the corresponding paramagnetic Curie temperatures. The effective g factor for all the compositions is approximately 2.0 (at $T > T_C$). In all cases, below that transition temperature, an abrupt increase in the effective resonant field, H_r, is observed (see Figure 9). For those temperatures, the curve is asymmetric (Dyson-like) and it can not be related to the g value.

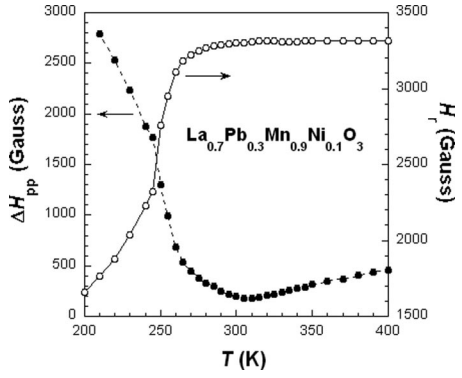

Figure 9. The linewidth and the magnetic field at which the absorption is maximum for the sample containing 10% Ni.

We have also checked the double integral of the resonance signal above magnetic order temperatures (in the paramagnetic regime) and found that it follows Arrhenius behaviour [Equation (4)].

$$I = I_0 e^{\Delta E/k_B T} \quad (4)$$

where I is the intensity extracted from the resonance line, I_0 is a fitting parameter and ΔE is the thermal activation energy for the dissociation of spin clusters.

This law allowed us to determine activation energy values of several meV for all the samples; their magnitudes decrease as Ni content increases (from 0.24 eV for x = 0.1 to 0.16 eV for x = 0.3). This ΔE value gives an idea about the strength of the correlation between spins or spin systems (clusters, if they are present) in the compound.

Regarding this Arrhenius behaviour we can correlate the activation energy trend (or loss of magnetic correlation) with the intrinsic resistivity measured in these compounds,

through the double exchange interaction mechanism. As pointed out by Oseroff et al., such correlation is widely found in practice, while no explanation for it is given in ref.[37] We can explain, at least qualitatively, these facts by assuming that the lowering of the activation energy runs parallel to a greater number of spin inversions in the ferromagnetic chain and therefore gives rise to a hindering of the electron transport along these structures. This happens because the same double-exchange-mediating electrons are the carriers of the electric current, as demonstrated by the simultaneous appearance of ferromagnetism and metallic character in these magnetoresistive perovskite-like compounds. So, as expected, we found that the lower the obtained dissociation energy, the smaller will be the electrical conductivity or higher the corresponding resistivity value (see Table 2).

From all previous experimental evidence, we propose a scenario in which the Ni cations enter as Ni^{3+} (LS) in a quite uniform way into the structure of the $La_{0.7}Pb_{0.3}MnO_3$ perovskite-like compounds when substituting Mn by Ni in percentages up to 30%. The samples behave as homogeneous granular materials, with crystallographic grain sizes about 20–45 nm. Magnetic and transport properties are determined by a weaker double exchange mechanism as the Ni content increases in the composition of the samples. All interactions appear to be ferromagnetic, of the Mn^{3+}–O^{2-}–Mn^{4+}, Mn^{3+}–O^{2-}–Ni^{3+} or Ni^{3+}–O^{2-}–Ni^{3+} type, in clear contrast with the cases of doping with Fe [antiferromagnetic coupling of Fe^{3+}(HS) to Mn, and spin-glass behaviour already for $x = 0.2$ (13)] or Co [with coexistence of Co^{3+}(LS) and Co^{4+}(HS), with clustering of Co^{3+} around Co^{4+} ions for $x = 0.3$[14]].

Conclusions

In the light of our experimental work, we can conclude that Ni enters into the $La_{0.7}Pb_{0.3}Mn_{1-x}Ni_xO_3$ family of perovskites as Ni^{3+} ions. Doping levels up to 30% only generate low distortion in the structure of these compounds. The measured low-temperature saturation magnetic moments are mainly due to the different magnetic moments of this ion, Ni^{3+}(LS) ferromagnetically coupled to Mn ions. A progressive increase in the doping level of Ni weakens the DE strength, giving rise to a subsequent decrease in both the measured low-temperature magnetic moment and Curie temperature values.

As a result of the sol–gel fabrication process used, we have obtained very homogeneous and small-size grains (about 20–45 nm) for all samples. This causes the products obtained to behave as homogeneous granular compounds. The measured resistivity behaviour at low temperatures is fully determined by the intergrain carrier tunnelling mechanism (which is especially evident for the 10% Ni-containing composition) that evolves to strong Coulomb blockade for the 20% Ni-doped sample.

All compounds show magnetoresistance with magnitudes, at the Curie temperatures, of 28 and 46% for the 30 and 10% Ni-doped samples, respectively.

Experimental Section

Mixed oxides of nominal composition $La_{0.7}Pb_{0.3}(Mn_{1-x}Ni_x)O_3$ ($0 \leq x \leq 0.3$) were prepared by the sol–gel method with the required quantities of analytical grade of La_2O_3, $Pb(NO_3)_2$, $Ni(NO_3)_2{\cdot}2H_2O$ and $Mn(C_2H_3O_2)_2{\cdot}4H_2O$ as the starting materials. Citric acid and ethylene glycol were used as gelling agents for the metallic ions in a nitrate solution. After drying in a sand bath for 24 h, the gel obtained was subjected to successive heat treatments at temperatures of 773, 973, and 1073 K, each for 10 h. In order to measure the electrical resistivities of the samples, the powder thus obtained was pelletized with a pressure of 7.2 MPa prior to final sintering at 1173 K for 10 h in flowing oxygen.

The first crystallographic characterization of the phases was performed by X-ray powder diffraction analysis by using a Philips X-Pert diffractometer working with Cu-K_α1 and Cu-K_α2 radiation, Soller slits of 0.04 rad and receiver and divergence slits of 1° (Table 3). Powder diffraction patterns were Rietveld-fitted by using the FULLPROF program.[40] The shape of the Bragg peaks was described by a pseudo-Voigt function. The background was modelled by using a linear interpolation function. From our structural fits and by using the Scherrer formula,[41] we have estimated a crystallographic grain size between 35–45 nm.

Table 3. Atomic parameters for the $La_{0.7}Pb_{0.3}(Mn_{1-x}Ni_x)O_3$ ($0.1 \leq x \leq 0.3$) family of compounds after the Rietveld refinements of the D1B neutron powder diffraction data. La and Pb atoms are at 6a-positions (0, 0, 1/4); Mn and Ni atoms are at 6b- (0, 0, 0) and O atoms are at 18e-positions (x, 0, 1/4). $Z = 6$ in all cases.

Sample	Ni 0.1	Ni 0.2	Ni 0.3
T (K)	296	244	230
Space group	$R\bar{3}c$	$R\bar{3}c$	$R\bar{3}c$
a (Å)	5.492(1)	5.4906(9)	5.4882(9)
c (Å)	13.331(3)	13.3168(9)	13.2991(9)
V (Å^3)	348.2(1)	347.7(9)	346.9(9)
t	0.995	0.994	0.995
La B (Å^2)/F_{occ}	0.9(4)/0.123	0.2(3)/0.117	0.2(3)/0.097
Pb B (Å^2)/F_{occ}	0.9(4)/0.057	0.2(3)/0.050	0.2(3)/0.054
Mn B (Å^2)/F_{occ}	0.9(4)/0.167	0.2(3)/0.104	0.2(3)/0.052
Ni B (Å^2)/F_{occ}	0.9(4)/0.018	0.2(3)/0.022	0.2(3)/0.027
O x	0.4574(1)	0.4551(1)	0.4583(1)
O B (Å^2)/F_{occ}	1.6(4)/0.532	1.4(4)/0.500	1.4(4)/0.463
Mn/Ni–O (Å)	1.95 × 6	1.95 × 6	1.95 × 6
La/Pb–O (Å)	2.52 × 3	2.50 × 3	2.51 × 3
	2.74 × 6	2.74 × 6	2.73 × 6
	2.97 × 3	2.99 × 3	2.97 × 3
<La/Pb–O> (Å)	2.74	2.74	2.74
Mn/Ni–O–Mn/Ni (°)	166.8	165.5	166.5
O–Mn/Ni–O (°)	90.7	90.8	90.8
R_p (%)	3.15	3.77	3.54
R_{wp} (%)	4.33	5.13	4.90
Bragg R-factor	2.63	5.22	5.39
χ^2	1.79	3.48	3.16

Magnetic and resistance measurements were conducted in a Quantum Design MPMS-7 SQUID magnetometer. The zero-field cooling (ZFC) and field cooling (FC) curves were obtained under an applied field of 10 mT. The order temperature, T_C, was determined from the ZFC curves as the temperature where the minimum of the dM/dT derivative occurs. Hysteresis loops at 10 K and up to 7 Tesla were also obtained. The resistance and magnetoresistance vs. temperature measurements were taken by using a conventional dc four-wire system, with the magnetic field applied parallel to the current.

A Bruker ESP300 spectrometer operating at the X-band and equipped with standard Oxford low-temperature devices was used to record the ESR and FMR powder spectra of the samples between 4.2 and 300 K. The magnetic field was calibrated by an NMR probe, and the frequency inside the cavity was determined with a Hewlett–Packard 5352B microwave frequency counter.

Neutron diffraction measurements were performed at the high-flux reactor at the Institut Laue-Langevin, Grenoble, France. In order to trace the temperature dependence of the structural and magnetic properties, measurements were carried out on D1B. We used a wavelength of 2.519 Å to study the range $2\theta = 20°–100°$ at temperatures ranging from 10 to 300 K. The Rietveld analysis of the diffraction data was performed by using the FULLPROF program. The line shape of the diffraction peaks was generated by a pseudo-Voigt function and the background interpolated between some fixed background points of the diagrams. In the final run, the following parameters were refined: unit-cell parameters, zero-point, half-width, pseudo-Voigt, and asymmetric parameters, scale factor, atomic coordinates, and thermal isotropic factors. The occupancy factors were also allowed to vary in the last steps of the refinements. Due to the high correlation between the thermal and occupancy factors, in some cases the refinements did not reach the convergence. In those cases, the occupancy factors were fixed to the theoretical ones.

Acknowledgments

The authors want to thank Prof. Evgeny Rozenberg for helpful discussions. We also want to thank the SGIKER for the Servicio de Medidas Magnéticas de la UPV/EHU. This work has been sponsored by the Spanish Ministerio de Ciencia y Tecnología under projects MAT2004-02425 and MAT2007-66737-C02–01.

[1] S. Jin, T. H. Tiefel, M. McCormack, R. A. Fastnacht, R. Ramesh, L. H. Chen, *Science* **1994**, *264*, 413.
[2] Y. Tokura (Ed.), *Colossal Magnetoresistive Oxides*, Gordon and Breach Science Publishers, **2000**.
[3] C. Zener, *Phys. Rev.* **1951**, *82*, 403–405.
[4] Y. Moritomo, A. Machida, K. Matsuda, M. Ichida, A. Nakamura, *Phys. Rev. B* **1997**, *56*, 5088–5091.
[5] P. W. Anderson, H. Hasewaga, *Phys. Rev.* **1995**, *100*, 675–677.
[6] K. Chahara, T. Ohno, M. Kasai, K. Kozono, *Appl. Phys. Lett.* **1993**, *63*, 1990–1992.
[7] P. G. Radaelli, M. Marezio, H. Y. Hwang, S. W. Cheong, B. Batlogg, *Phys. Rev. B.* **1996**, *54*, 8992–8995.
[8] L. Righi, P. Gorria, M. Insausti, J. Gutiérrez, J. M. Barandiarán, *J. Appl. Phys.* **1997**, *81*, 5767–5769.
[9] J. Gutiérrez, J. M. Barandiarán, M. Insausti, L. Lezama, A. Peña, J. J. Blanco, T. Rojo, *J. Appl. Phys.* **1998**, *83*, 7171–7173.
[10] M. Pissas, G. Kallias, E. Devlin, A. Simopoulos, D. Niarchos, *J. Appl. Phys.* **1997**, *81*, 5770–5772.
[11] K. H. Ahn, X. W. Wu, K. Liu, C. L. Chien, *Phys. Rev. B.* **1996**, *54*, 15299–15302.
[12] K. Ghosh, S. B. Ogale, R. Ramesh, R. L. Greene, T. Venkatesan, K. M. Gapchup,R. Bathe, S. I. Patil, *Phys. Rev. B* **1999**, *59*, 533–537.
[13] J. Gutiérrez, A. Peña, J. M. Barandiarán, J. L. Pizarro, T. Hernández, L. Lezama, M. Insausti, T. Rojo, *Phys. Rev. B* **2000**, *61*, 9028–9035.
[14] A. Peña, J. Gutiérrez, I. Gil de Muro, J. Campo, J. M. Barandiarán, T. Rojo, *Eur. J. Inorg. Chem.* **2006**, *16*, 3227–3235.
[15] J. B. Goodenough, A. Wold, R. J. Arnott, N. Menyuk, *Phys. Rev.* **1961**, 124, 373.
[16] G. Blasse, *J. Phys. Chem. Solids* **1965**, *26*, 1969.
[17] N. Y. Vasanthacharya, P. Ganguly, J. B. Goodenough, C. N. Rao, *J. Phys. C. Solid State Phys.* **1984**, 17, 2745; D. D. Sarma, O. Rader, T. Kachel, A. Chainani, M. Mathew, K. Holldack, W. Gudat, W. Eberhardt, *Phys. Rev. B* **1994**, 49, 14238.
[18] A. Wold, R. J. Arnott, *J. Phys. Chem. Solids* **1959**, *9*, 176; M. Sonobe, A. Kichizo, *J. Phys. Soc., Jpn.* **1992**, 61, 4193.
[19] J. Blasco, J. García, M. C. Sánchez, J. Campo, G. Subías, J. Pérez-Cacho, *Eur. Phys. J. B* **2002**, 30, 469.
[20] R. D. Shannon, *Acta Crystallogr., Sect. A* **1976**, *32*, 751.
[21] M. J. Martínez-Lope, M. T. Casais, J. A. Alonso, *J. Alloys Compd.* **1998**, *275*–277, 109–112.
[22] A. Arrott, *Phys. Rev.* **1957**, *108*, 1394–1396.
[23] J. Campo, J. Luzón, F. Palacio, A. Millán, G. J. McIntyre, *Polyhedron* **2003**, *22*, 2297–2299, and references therein.
[24] N. F. Mott, *J. Non-Cryst. Solids* **1968**, *1*, 1–17.
[25] J. Gutiérrez, A. Peña, J. M. Barandiarán, J. L. Pizarro, L. Lezama, M. Insausti, T. Rojo, *J. Phys.: Condens. Matter* **2000**, *12*, 10523–10534.
[26] H. Huhtinen, R. Laiho, K. G. Lisunov, V. N. Stamov, V. S. Zakhvalinskii, *J. Magn. Magn. Mater.* **2002**, 238, 160–167.
[27] A. L. Efros, B. L. Shklovskii, *J. Phys. C: Solid State Phys.* **1975**, *8*, L49.
[28] R. Mahendiran, R. Mahesh, A. K. Raychaudhuri, C. N. R. Rao, *Solid State Commun.* **1995**, *94*, 515–518.
[29] H. Song, W. J. Kim, S.-J. Kwon, *J. Magn. Magn. Mater.* **2000**, *213*, 126–134.
[30] Ll. Balcells, J. Fontcuberta, B. Martínez, X. Obradors, *Phys. Rev. B* **1998**, *58*, R14697–R14700.
[31] A. Peña, J. Gutiérrez, J. M. Barandiarán, J. P. Chapman, M. Insausti, T. Rojo, *J. Solid State Chem.* **2003**, 174, 52–59.
[32] S. E. Lofland, S. M. Bhagat, H. L. Ju, G. C. Xiong, T. Venkatesan, R. L. Greene, *Phys. Rev. B* **1995**, 52, 15058–15061.
[33] E. Rozenberg, M. Auslender, I. Felner, G. Gorodetsky, *J. Appl. Phys.* **2000**, 88, 2578, and references therein.
[34] M. García-Hernández, F. Guinea, A. de Andrés, J. L. Martínez, C. Prieto, L. Vázquez, *Phys. Rev. B* **2000**, 61, 9549–9552.
[35] P. Sheng, *Philos. Mag. B* **1992**, 65, 357.
[36] J. M. D. Coey, A. E. Berkowitz, Ll. Balcells, F. F. Putris, A. Barry, *Phys. Rev. Lett.* **1998**, *80*, 3815–3818.
[37] S. B. Oseroff, M. Torikachvili, J. Singley, S. Ali, S-W. Cheong, S. Schultz, *Phys. Rev. B* **1996**, 53, 6521.
[38] M. Domínguez, S. E. Lofland, S. M. Baghat, A. K. Raychaudhuri, H. L. Hu, T. Venkatesan, R. L. Greene, *Solid State Commun.* **1996**, *97*, 193.
[39] S. E. Lofland, P. Kim, P. Dahiroc, S. M. Baghat, S. D. Tyagi, S. G. Karabashev, D. A. Shulyatev, A. A. Arsenov, Y. Mukovskii, *Phys. Lett. A* **1997**, 233, 476.
[40] J. Rodríguez-Carvajal, computer code FULLPROF, Rietveld Pattern Matching Analysis of Powder Patterns, ILL, Grenoble, **1990**.
[41] B. E. Warren (Ed.), *X-ray Diffraction: Diffraction by Imperfect Crystals*, Dover Publications, Inc., New York, USA, **1969**.

Received: October 31, 2007
Published Online: April 23, 2008

